Facet-switching of rate-determining step on copper in CO₂-to-ethylene electroreduction

Yu-Cai Zhang[a,1] (ID), Xiao-Long Zhang[a,1] (ID), Zhi-Zheng Wu[a,1] (ID), Zhuang-Zhuang Niu[a] (ID), Li-Ping Chi[a] (ID), Fei-Yue Gao[a] (ID), Peng-Peng Yang[a] (ID), Ye-Hua Wang[a] (ID), Peng-Cheng Yu[a] (ID), Jing-Wen Duanmu[a] (ID), Shu-Ping Sun[a] (ID), and Min-Rui Gao[a,2] (ID)

Reduction of carbon dioxide (CO_2) by renewable electricity to produce multicarbon chemicals, such as ethylene (C_2H_4), continues to be a challenge because of insufficient Faradaic efficiency, low production rates, and complex mechanistic pathways. Here, we report that the rate-determining steps (RDS) on common copper (Cu) surfaces diverge in CO_2 electroreduction, leading to distinct catalytic performances. Through a combination of experimental and computational studies, we reveal that C—C bond-making is the RDS on Cu(100), whereas the protonation of *CO with adsorbed water becomes rate-limiting on Cu(111) with a higher energy barrier. On an oxide-derived Cu(100)-dominant Cu catalyst, we reach a high C_2H_4 Faradaic efficiency of 72%, partial current density of 359 mA cm^{-2}, and long-term stability exceeding 100 h at 500 mA cm^{-2}, greatly outperforming its Cu(111)-rich counterpart. We further demonstrate constant C_2H_4 selectivity of >60% over 70 h in a membrane electrode assembly electrolyzer with a full-cell energy efficiency of 23.4%.

CO_2 electroreduction | rate-determining step | facet | ethylene | selectivity and long-term stability

Ethylene (C_2H_4) has a global market volume of around 224 million tons in 2022, far exceeding that of any other organic chemical demanded annually (1). It is an important industrial building block to make various plastics, cosmetics, and solvents. Traditional production of C_2H_4 was relied on steam cracking of long-chain hydrocarbons (e.g., naphtha or liquefied petroleum gas); this process, unfortunately, releases more than 200 million tons of carbon dioxide (CO_2) per year, contributing approximately 0.6% of total anthropogenic CO_2 emissions (2, 3). The electrochemical CO_2 reduction (CO_2R) with water using renewable electricity offers a promising path for low-carbon C_2H_4 production (4–9). Performance of the CO_2-to-C_2H_4 electroreduction has progressed substantially over past years via tuning of catalyst morphology (10), oxidation state (11), facets (12) and defects (13), introduction of molecules (14) and halogens (15), alloying of copper (Cu) with other metals (16), and use of cascade CO_2 electroreduction (17). In alkaline media, peak Faradaic efficiencies (FE) of 70% and >80% have been reported over abrupt Cu interface (18) and Cu-Al alloy (16), respectively, but operating in alkali imposes a low carbon utilization efficiency. Recently, CO_2-to-C_2H_4 electroreduction in mild neutral electrolytes has shown impressive FEs on some Cu-based catalysts (19–22); however, only a few of these catalysts were demonstrated to exhibit a high partial current density of >300 mA cm^{-2}. Moreover, their performances in realistic membrane electrode assembly (MEA) electrolyzer are sparsely explored (23).

To put commercial-scale electrosynthesis of C_2H_4 into perspective, research efforts should be devoted to not only new catalyst design but also mechanistic understanding that governs the CO_2R properties. At present, the mechanism of the reaction pathway toward multicarbon (C_{2+}) products remains a matter of ongoing debate (24–26). One critical issue is whether C—C coupling or the protonation of *CO to *CHO is the rate-determining step (RDS). Over Cu catalysts, Xu and coworkers proposed recently that the protonation of *CO with adsorbed water was the RDS during CO electroreduction in the formation of C_{2+} products (25). In contrast to this proposal, however, Kastlunger et al. reported that C—C bond-making was energetically favored as RDS in the electrochemical CO-to-C_{2+} conversion according to joint computational and experimental studies (26). During CO_2R on Cu, it has widely been thought that C—C coupling-a pH-independent process-is the RDS for C_{2+} product formation (27–31). Nevertheless, the RDS of C_{2+} formation on a Cu catalyst in principle can also be the protonation of *CO with adsorbed water, which shows a pH-independent reaction rate as well (24). Identifying the exact rate-limiting CO_2R step on Cu will provide foundational insight into catalyst development, which, however, has been poorly investigated thus far (32).

Significance

We experimentally show that the rate-determining step (RDS) on common copper (Cu) surfaces diverge in CO_2 electroreduction, leading to distinct catalytic performance. The C—C bond-making is the RDS on Cu(100), whereas the protonation of *CO with water becomes RDS on Cu(111). On an oxide-derived Cu(100)-dominant Cu catalyst, we reach a high C_2H_4 Faradaic efficiency of 72% (C_{2+} Faradaic efficiency of about 90%), partial current density of 359 mA cm^{-2}, and long-term stability exceeding 100 h.

Here, we combined in situ spectroscopic studies with electrokinetic measurements and density functional theory (DFT) calculations and observed a RDS transition from the protonation of *CO with adsorbed water on Cu(111)-dominant Cu to the C—C coupling step on Cu(100)-dominant Cu catalyst. Our results further reveal that the rate-limiting barrier of C—C coupling on Cu(100) is considerably lower than the protonation of *CO taking place on Cu(111). As a result, we achieved efficient CO_2-to-C_2H_4 conversion on Cu(100)-dominant Cu with a partial current density of 359 mA cm^{-2}, FE of 72%, and a half-cell C_2H_4 power conversion efficiency (PCE) of 33%, far surpassing the metrics obtained on Cu(111)-dominant counterpart.

Results and Discussion

Catalyst Synthesis and Characterizations. Copper nanostructures with different facets have been well studied for catalyzing CO_2R (33–39). As previously demonstrated, Cu(100) can facilitate C_2H_4 formation more efficiently than Cu(111) (34). Compared with the close-packed Cu(111) surface, the low-coordination Cu(100) enables superior adsorption of *CO and thus a higher *CO coverage (35), which improves the reaction kinetics for C—C coupling. Nevertheless, prior studies (36, 37) also report that a noticeable amount of C_{2+} products (FE > 50%) can form on Cu(111), so this surface would be chemically active for CO-to-C_{2+} conversion as well. Today, the inferior C_{2+} selectivity on Cu(111) was caused by slow C—C coupling kinetics or by

proceeding with a different mechanistic pathway is unclear (38, 39).

We worked with copper oxide (CuO) nanosheets as a precursor because oxygen vacancies can be made on this structure (40). Oxygen vacancies were shown to be effective for adsorbing *CO during CO_2R that mediates the formation of Cu(100) facets (12, 41). Additionally, such a two-dimensional sheet-like structure can provide maximum surface to expose desired Cu facets. We synthesized original CuO (termed o-CuO) nanosheets using a method described previously (42). The obtained sample then underwent a nitrogen plasma irradiation at 100 W for 30 min (Fig. 1A). High-angle annular dark-field scanning transmission electron microscopy (HAADF-STEM) images exhibited that the plasma-treated CuO (termed p-CuO) well inherited the sheet-like morphology of o-CuO (Fig. 1 B and C and *SI Appendix*, Figs. S1–S7). The thickness of o-CuO nanosheets, ~7 nm as determined by atomic force microscopy (AFM) (Fig. 1D), remained almost unchanged after plasma treatment (Fig. 1E). Kelvin probe force microscopy showed that the contact potential difference (CPD) value of o-CuO reduced by ~438 mV after plasma irradiation (Fig. 1 F–H). The lower CPD of p-CuO hints at a smaller work function, which might be caused by the formation of oxygen vacancies that modulate the density of states near the Fermi level (43, 44). The existence of structural defects was characterized by small angle X-ray scattering (*SI Appendix*, Fig. S8), yielding surface fractal (D_s) of 2.29 for o-CuO, which is smaller than that of 2.56 for p-CuO (Fig. 1I), suggesting more defects in p-CuO (44).
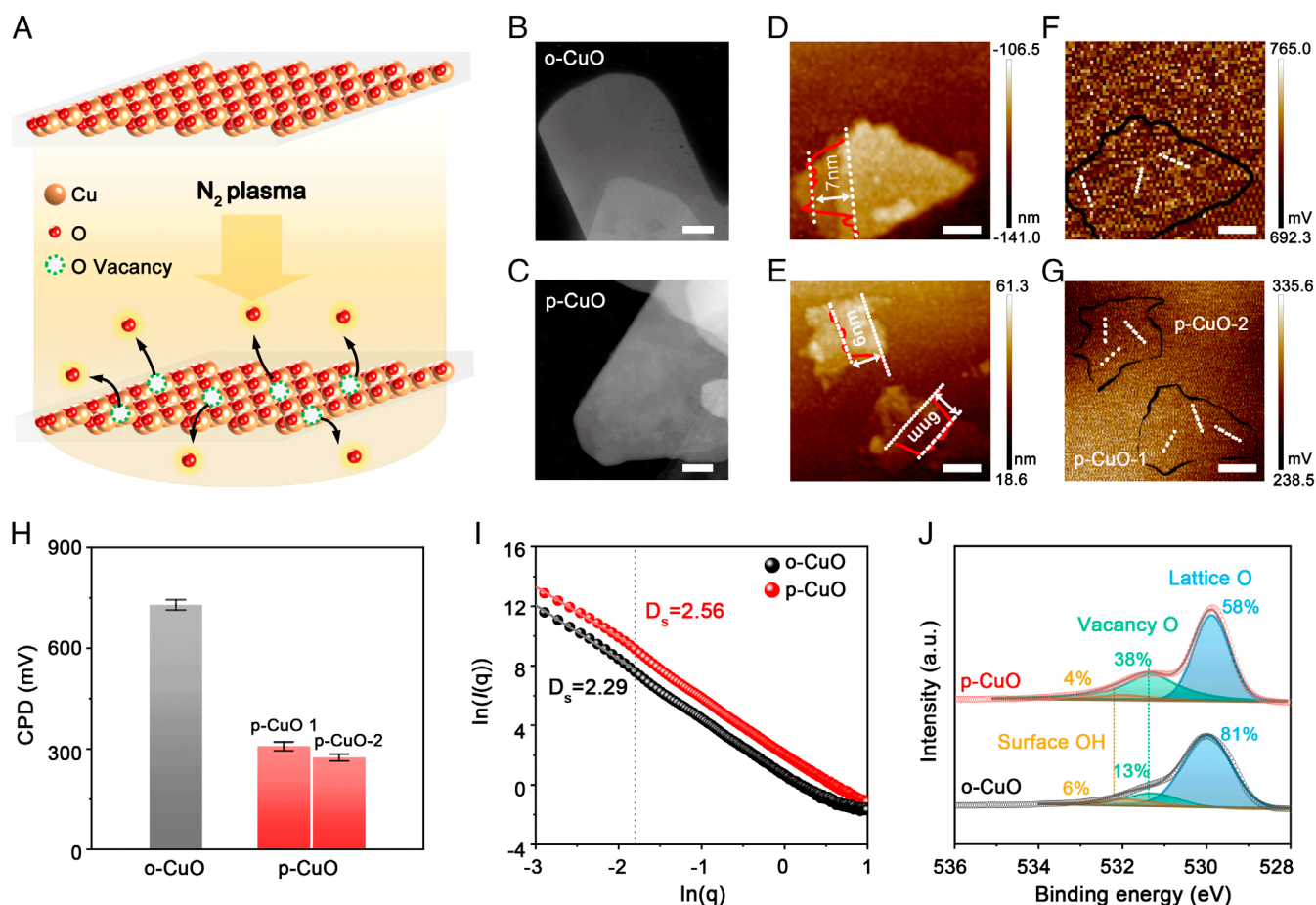

Fig. 1. Synthesis and structural characterization of o-CuO and p-CuO nanosheets. (*A*) Schematic illustration of the synthesis of p-CuO. (*B* and *C*) HAADF-STEM images of o-CuO (*B*) and p-CuO (*C*). (Scale bar, 50 nm.) (*D* and *E*) Topography images for o-CuO (*D*) and p-CuO (*E*). (Scale bar, 200 nm.) (*F* and *G*) CPD images for o-CuO (*F*) and p-CuO (*G*). (Scale bar, 200 nm.) (*H*) CPD values obtained from different regions of o-CuO and p-CuO shown in (*F*) and (*G*). Error bars are based on the SD of three individual measurements. (*I*) ln(*I*(q)) versus ln(q) plots of the catalysts derived from the small angle X-ray scattering data (*SI Appendix*, Fig. S8). (*J*) O 1 s XPS spectra of o-CuO and p-CuO.

Furthermore, X-ray photoelectron spectroscopy (XPS; Fig. 1*J*), electron paramagnetic resonance (EPR; *SI Appendix*, Fig. S9), and X-ray absorption spectroscopy (XAS; *SI Appendix*, Fig. S10) all confirmed the introduction of abundant oxygen vacancies in p-CuO.

In Fig. 2*A*, DFT calculations predict that the adsorption energy of the *CO on p-CuO(001) is greater by 0.34 eV than that on o-CuO, so that the presence of oxygen vacancies should lead to superior *CO adsorption, consistent with prior reports (41). Moreover, although Cu(111) is the most stable facet in polycrystalline Cu, our DFT calculations predict that the formation of Cu(100) is more favored in the presence of *CO (Fig. 2*B* and *SI Appendix*, Fig. S11). This result indicates that *CO intermediates can engineer the Cu facets, in agreement with recent observation (12). Taken together, the DFT results suggest that p-CuO with oxygen vacancies preferentially exposes Cu(100) facets via

*CO modulation during CO$_2$R, whereas the o-CuO would be reduced to Cu(111).

To validate experimentally the predictions, the two CuO nanosheet dispersions were sprayed onto the gas diffusion layer (GDL) and then experienced an electrochemical reduction process (*Materials and Methods*). XPS analysis of the reduced o-CuO and p-CuO (termed o-Cu and p-Cu hereafter) showed that both samples were metallic in nature (*SI Appendix*, Fig. S12) without oxidation signals detected. EPR results showed that no oxygen vacancy can be detected (*SI Appendix*, Fig. S13). Transmission electron microscopy (TEM) images of o-Cu and p-Cu revealed that the sheet-like morphologies retained after reducing treatment (Fig. 2 *C* and *D*). The selected-area electron diffractions of o-Cu and p-Cu showed their single crystalline feature and were consistent with the diffraction patterns from the [111] and [001] zone axes of o-Cu and p-Cu with face-centered cubic phase (*Insets* in
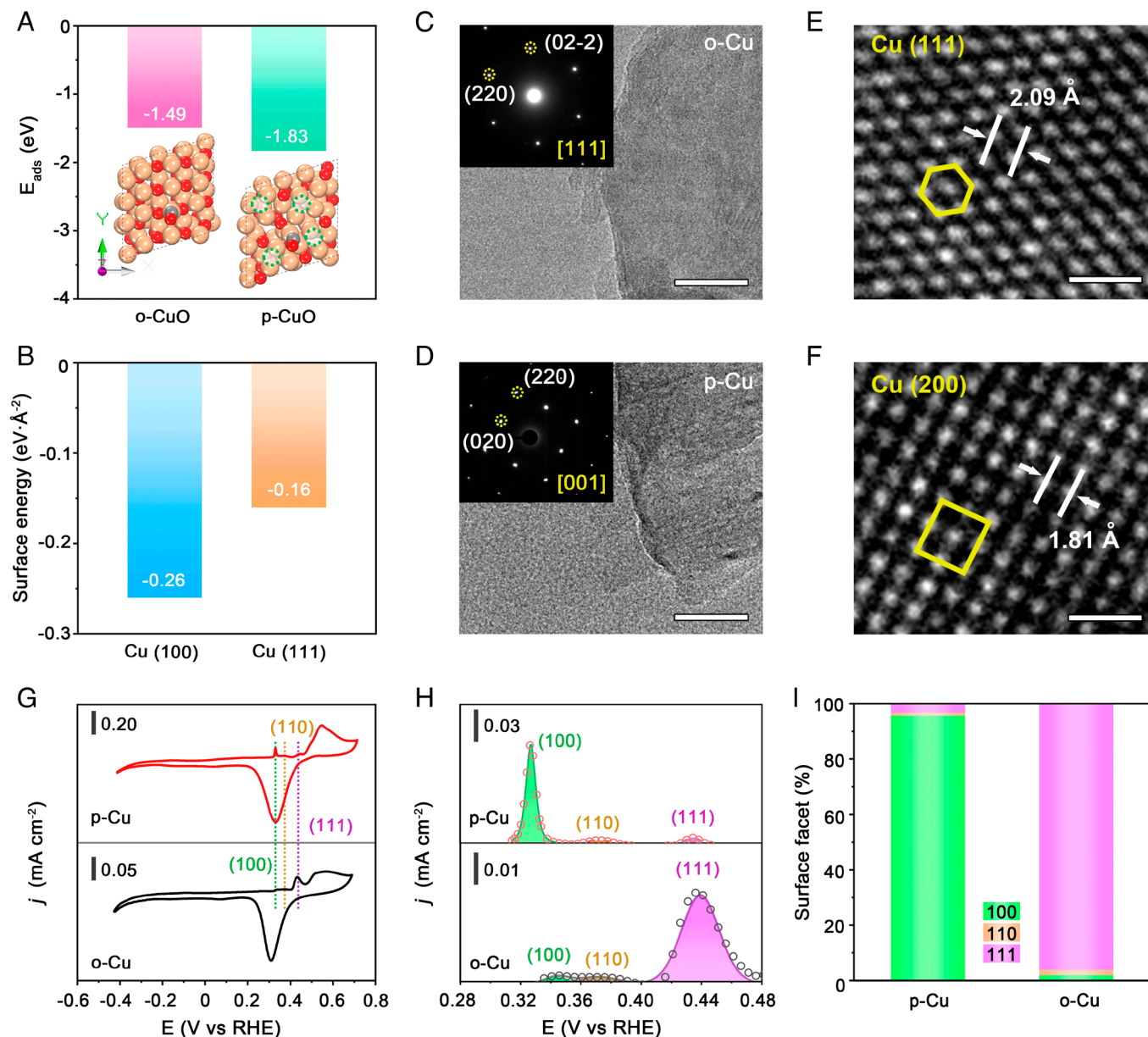

Fig. 2. Surface analysis of different catalysts. (*A*) The adsorption energy of *CO on o-CuO and p-CuO. (*B*) Surface energy of Cu(100) and Cu(111) with adsorption of CO intermediates. (*C* and *D*) HRTEM images of o-Cu (*C*) and p-Cu (*D*). (Scale bars, 20 nm.) *Insets* in (*C*) and (*D*) are the corresponding SAED patterns. (*E* and *F*) Atomic-resolution HRTEM images of the o-Cu (*E*) and p-Cu (*F*). (Scale bars, 0.5 nm.) The yellow boxes represent the arrangement of atoms. (*G*) CV curves of o-Cu and p-Cu in 1 M KOH. Scan rate: 20 mV s^{-1}. (*H*) Fitted OH$^-$ adsorption peaks of o-Cu and p-Cu. (*I*) The radio of Cu(100), Cu(110), and Cu(111) facets, quantified by the OH$^-$ electroadsorption.

Fig. 2 *C* and *D*), respectively. A high-resolution TEM (HRTEM) image of the o-Cu exhibited the atomic arrangement of the atoms on the (111) planes (Fig. 2*E* and *SI Appendix*, Fig. S14), whereas the p-Cu exposes lattice fringes of 1.81 Å, corresponding to (200) planes of Cu (Fig. 2*F* and *SI Appendix*, Fig. S15).

In Fig. 2*G*, we turn to use surface-sensitive electrochemical techniques to provide further facet information on the oxide-derived o-Cu and p-Cu. Given the facet-dependent OH^- adsorption feature (i.e., $Cu + OH^- \rightarrow Cu(OH)_{ad} + e^-$) (22), we thus studied the electrochemical adsorption of OH^- on the two catalysts. Cyclic voltammetry measurement (Fig. 2*G*) on o-Cu showed one prominent peak at ~0.44 versus the reversible hydrogen electrode (RHE; all potentials are versus RHE hereafter unless noted otherwise), corresponding to the OH^- adsorption on Cu(111), whereas the cyclic voltammetry from p-Cu displayed one prominent peak at ~0.33 V, in agreement with OH^- adsorption on Cu(100) facets (45). Quantification of the percentage of the two facets via

integrating the $Cu(OH)_{ad}$ peaks yielded 96.2% Cu(111) on o-Cu and 95.7% Cu(100) on p-Cu (Fig. 2 *H* and *I*). Our quantitative analysis further showed that the formation of Cu(110) facets during CO_2R is very limited, mere 2.0% for o-Cu and 1.1% for p-Cu. These results agree well with the surface features probed by the lead underpotential deposition technique (*SI Appendix*, Fig. S16). In addition, X-ray diffraction (XRD) patterns showed that the strongest diffractions for o-Cu and p-Cu were at 43.3° and 50.4°, indicating the preferential exposure of (111) and (100) facets, respectively (*SI Appendix*, Fig. S17). These results, together with structural characterizations above, confirm that o-Cu is dominated by (111), while p-Cu mainly exposes (100).

Electrochemical CO_2R Performance. We evaluated the CO_2R performance of the o-Cu and p-Cu catalysts at current densities of 100–700 mA cm^{-2} in 1 M KCl (pH ~ 6.8) in a flow cell (*Materials and Methods*). As shown in Fig. 3*A*, the p-Cu catalyst
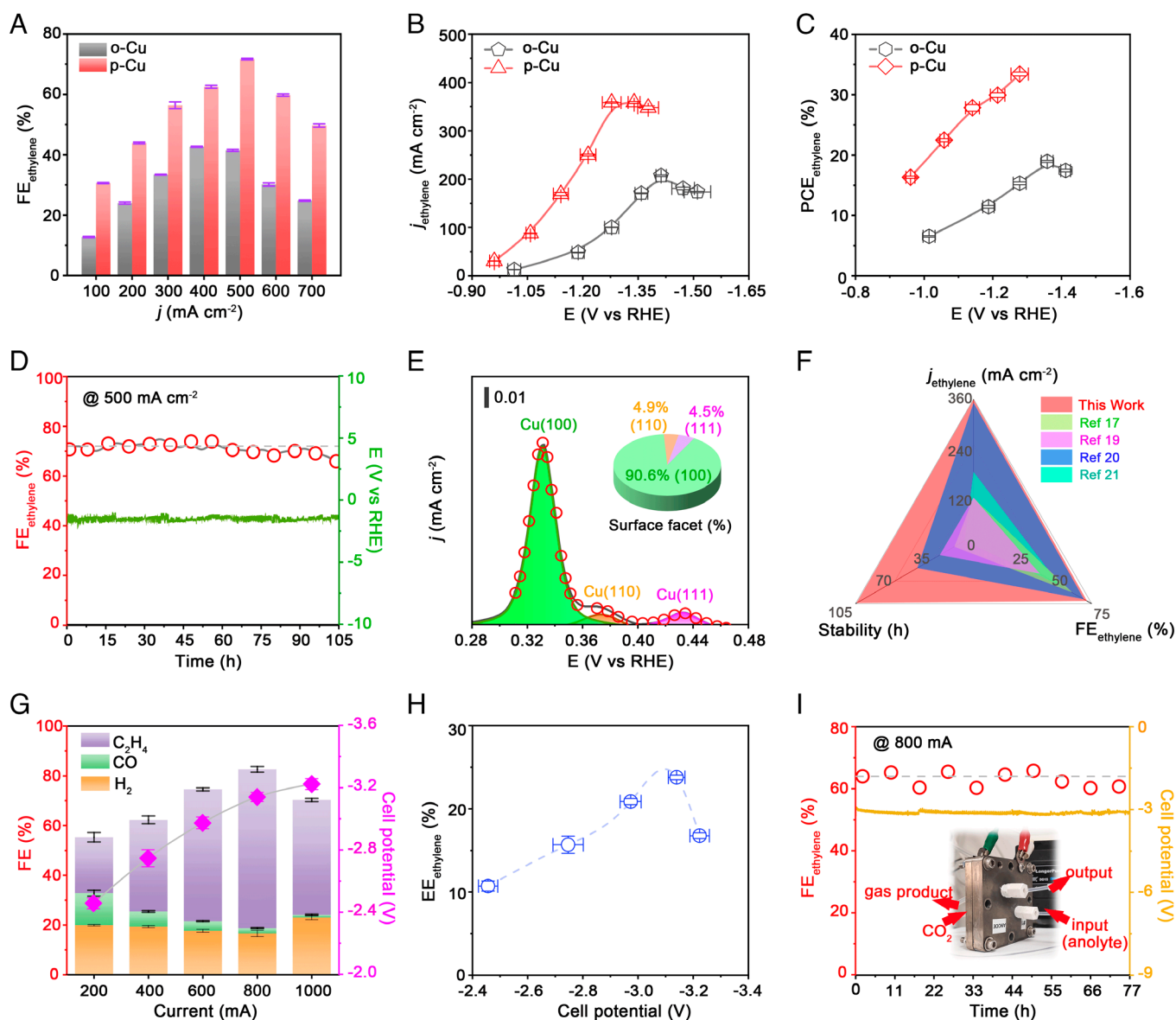

Fig. 3. CO_2R performance in the flow cell and MEA electrolyzer. (*A*) FE of C_2H_4 on o-Cu and p-Cu electrodes versus different applied current densities. (*B*) Partial current densities of C_2H_4 on o-Cu and p-Cu electrodes versus different applied potentials. (*C*) Half-cell PCE of C_2H_4 on o-Cu and p-Cu electrodes versus different applied potentials. (*D*) Stability test of p-Cu electrode at 500 mA cm^{-2}. (*E*) Fitted OH^- adsorption peaks of the spent p-Cu after the stability test. *Insets* show the percentage of different facets. (*F*) Comparison of C_2H_4 FEs, C_2H_4 partial current densities, and long-term stability for various Cu electrodes reported in the literature under neutral operating environments. (*G*) FE of C_2H_4 and full cell potential on p-Cu electrodes versus applied currents. (*H*) Energy efficiency of C_2H_4 on p-Cu electrodes versus applied voltages. (*I*) Stability test of the p-Cu electrode in a 5 cm^{-2} MEA electrolyzer at total current of 800 mA. The anode electrolyte is 0.1 M $KHCO_3$. The *Inset* shows the photograph of the MEA electrolyzer. Error bars are based on the SD of three independent measurements.

attained higher C_2H_4 FEs than that of o-Cu at all current densities examined (*SI Appendix*, Fig. S18 and Tables S1 and S2). At 500 mA cm^{-2}, p-Cu attained a C_2H_4 FE of 72% (C_{2+} FE of 90%), whereas o-Cu attained only 40% (C_{2+} FE of 59%) under the same testing conditions. We achieved a maximum C_2H_4 partial current density of 359 mA cm^{-2} on p-Cu at –1.28 V, which is 1.7-fold higher than on o-Cu at –1.41 V (Fig. 3*B*). Additionally, our optimal flow reactor exhibited a half-cell C_2H_4 PCE (water oxidation reaction at the anode) of up to 33% (Fig. 3*C*), greatly surpassing that obtained on o-Cu and is among the best values reported previously (*SI Appendix*, Fig. S19).

The p-Cu catalyst showed a C_2H_4 FE of ~70% with mere slight change over 100 h in the flow reactor (Fig. 3*D*). Surface-sensitive electrochemical measurements demonstrated that the surface of the spent p-Cu was still dominated by (100) facet (>90%; Fig. 3*E*), consistent with the postmortem TEM and SAED analyses (*SI Appendix*, Fig. S20). Fig. 3*F* compares the performance metrics of the p-Cu catalyst with those reported previously in terms of C_2H_4 FE, partial current densities, and operating stability. Our results obtained on p-Cu represent the best performance documented under similar testing conditions (*SI Appendix*, Table. S3).

In Fig. 3*G*, we examined the potential of the p-Cu catalyst for realistic use in a MEA electrolyzer (*SI Appendix*, Fig. S21) (overall reaction: $2CO_2 + 2H_2O \rightarrow C_2H_4 + 3O_2$), which yielded a maximum C_2H_4 FE of 64%, and the H_2 evolution was suppressed to ~17% (*SI Appendix*, Table S4). At a full-cell voltage of 3.14 V, the energy efficiency (EE) toward C_2H_4 was determined to be 23.4% (Fig. 3*H*). At 800 mA, our MEA electrolyzer assembled by this catalyst can produce C_2H_4 steadily with selectivity of >60% for at least 70 h (Fig. 3*I* and *SI Appendix*, Fig. S22 and Table S5).

Facet-Dependent RDS on Cu Catalysts. Our o-Cu and p-Cu catalysts, both of which were derived from CuO nanosheets, provide an ideal catalyst platform to probe the cause of the distinct CO_2-to-C_2H_4 properties because they can exclude the effects of morphologies, surface area, and oxidation states. Seeking to understand the source of facet-dependent performance, in situ spectroscopic studies and electrokinetic analyses were conducted. In situ Raman measurements on o-Cu (Fig. 4*A*) and p-Cu (Fig. 4*B*) both showed two peaks at ~280 and ~360 cm^{-1} as CO_2R proceeds, which were attributed to the Cu-CO rotation (P1) and Cu-CO stretching (P2) bands, respectively (46). The P2/P1 ratio was previously reported by Zhan et al. as a valid measure of the *CO coverage on Cu during CO_2R (47). A quantitative analysis revealed a much higher P2/P1 ratio for p-Cu than that for o-Cu (Fig. 4*C*), indicating greater *CO coverage on the p-Cu surface. This could be the result of stronger adsorption of *CO intermediates over p-Cu, as confirmed by the CO stripping experiments (Fig. 4*D*).

In situ Raman spectroscopy of o-Cu during CO_2R at high-wavenumber modes showed bias-dependent Raman peaks corresponding to bridge-bound CO (*CO$_{bridge}$) at about ~1,840 cm^{-1} and atop-bound CO (*CO$_{atop}$) at ~2,054 cm^{-1} (Fig. 4*E*) (48). The more prominent *CO$_{bridge}$ peaks in Fig. 4*E* give a strong indication that o-Cu favors bridge CO rather than atop CO. On p-Cu, we however found that the bridge CO was overwhelmingly suppressed and the atop-bound CO became dominant as the applied potential increases (Fig. 4*F*), implying that Cu(100) are more favorable sites for *CO$_{atop}$ formation.

In Fig. 4*G*, we measured and compared the reaction order of CO for C_2H_4 formation (24), yielding reaction orders of first for o-Cu and second for p-Cu (*SI Appendix*, Tables S6 and S7). The results strongly indicated that C—C coupling is the RDS on p-Cu, whereas on o-Cu the protonation of *CO with adsorbed H_2O to

*CHO turns to be possible RDS, consistent with Tafel slopes of ~120 mV dec^{-1} (*SI Appendix*, Fig. S23 and Tables S8 and S9)-the first electron transfer being the RDS (49)-obtained on both catalysts. To test whether RDS on o-Cu involves H_2O dissociation, we measured the kinetic isotopic effect (KIE) of H/D, i.e., the ratio of C_2H_4 formation rates in H_2O and D_2O (*Materials and Methods*), which yielded a KIE value of 1.9 on o-Cu and of 1.1 on p-Cu (Fig. 4*H* and *SI Appendix*, Tables S10 and S11). The H/D ratio of 1.9 obtained on o-Cu implies that H_2O dissociation occurs in the RDS (15, 50). In contrast, on p-Cu, the RDS should not involve H_2O dissociation owing to its KIE value close to 1. We further revealed, from in situ differential electrochemical mass spectroscopy (DEMS), that p-Cu exhibits a notable mass to charge signal (*m/z*) for C_2H_4 ($C_2H_2^+$, *m/z* = 26) at –0.51 V, in comparison to that at much more negative potential of –1.04 V on o-Cu (Fig. 4*I* and *SI Appendix*, Fig. S24). As previously thought (34, 51), C_2H_4 produced at low overpotentials follows the Eley-Rideal mechanism with C—C coupling as the RDS. Under high overpotentials, however, H_2O dissociation by $H_2O + e^- \rightarrow OH^- + *H$ would proceed, causing the protonation of *CO to be rate-limiting.

Altogether, our entire results reveal a facet-dependent RDS on Cu that determines the CO_2-to-C_2H_4 performances. On (111)-dominant o-Cu, the surface coverage of *CO is low and such key intermediate mostly adopts the bridge-bound configuration, resulting in a reaction pathway with RDS different from C—C coupling. Our experimental data indicate that the DRS on o-Cu involves H_2O dissociation and the reaction order of CO for C_2H_4 approaches 1. These infer reasonably that the protonation of *CO with adsorbed H_2O via a proton-coupled electron transfer (PCET) step to *CHO should be the RDS on o-Cu, as depicted in Fig. 5*A*. In stark contrast, the (100)-dominant p-Cu possesses surface sites favorable for *CO$_{atop}$ adsorption and shows a high *CO coverage. Over this catalyst, the major impediment to synthesizing C_2H_4 from CO_2 turns out to be the coupling of two *CO adsorbates (Fig. 5*A*), which was evidenced by the second reaction order, KIE and DEMS results shown above. The sufficient surface coverage of *CO on p-Cu promotes the rate of C—C coupling, leading to the notable CO_2-to-C_2H_4 performance.

To gain further insight into the catalytic mechanisms, we calculated the reaction-free energies of the *CO→*OCCO and *CO→*CHO pathways on Cu(100) and Cu(111) facets, respectively (*Materials and Methods*). The energy diagrams and images of the initial, transition, and final states are exhibited in Fig. 5 *B* and *C*. On Cu(100), the calculated activation energy barrier for *CO→*OCCO is much lower than that for *CO→*CHO, suggesting that the protonation of *CO to *CHO is kinetically prohibited on this facet whereas C—C coupling is favored. The calculations further predict that, on Cu(111), the energy barrier for *CO→*CHO lies below for *CO→*OCCO so that the protonation of *CO becomes kinetically preferred on this close-packed surface. Additionally, Fig. 5 *B* and *C* also show that *CO→*OCCO occurs on Cu(100) requires less energy than *CO→*CHO on Cu(111), which explains the superior CO_2-to-C_2H_4 conversion obtained on (100)-dominant p-Cu, in agreement with other observations (12, 22, 52, 53).

Discussion

To conclude, we have demonstrated that CuO nanosheets with and without oxygen vacancies are efficient precursors to generate Cu catalysts that preferentially expose Cu(100) and Cu(111) facets, respectively, under reducing conditions. We found that the RDS in CO_2R is the C—C bond formation on Cu(100)-dominant Cu
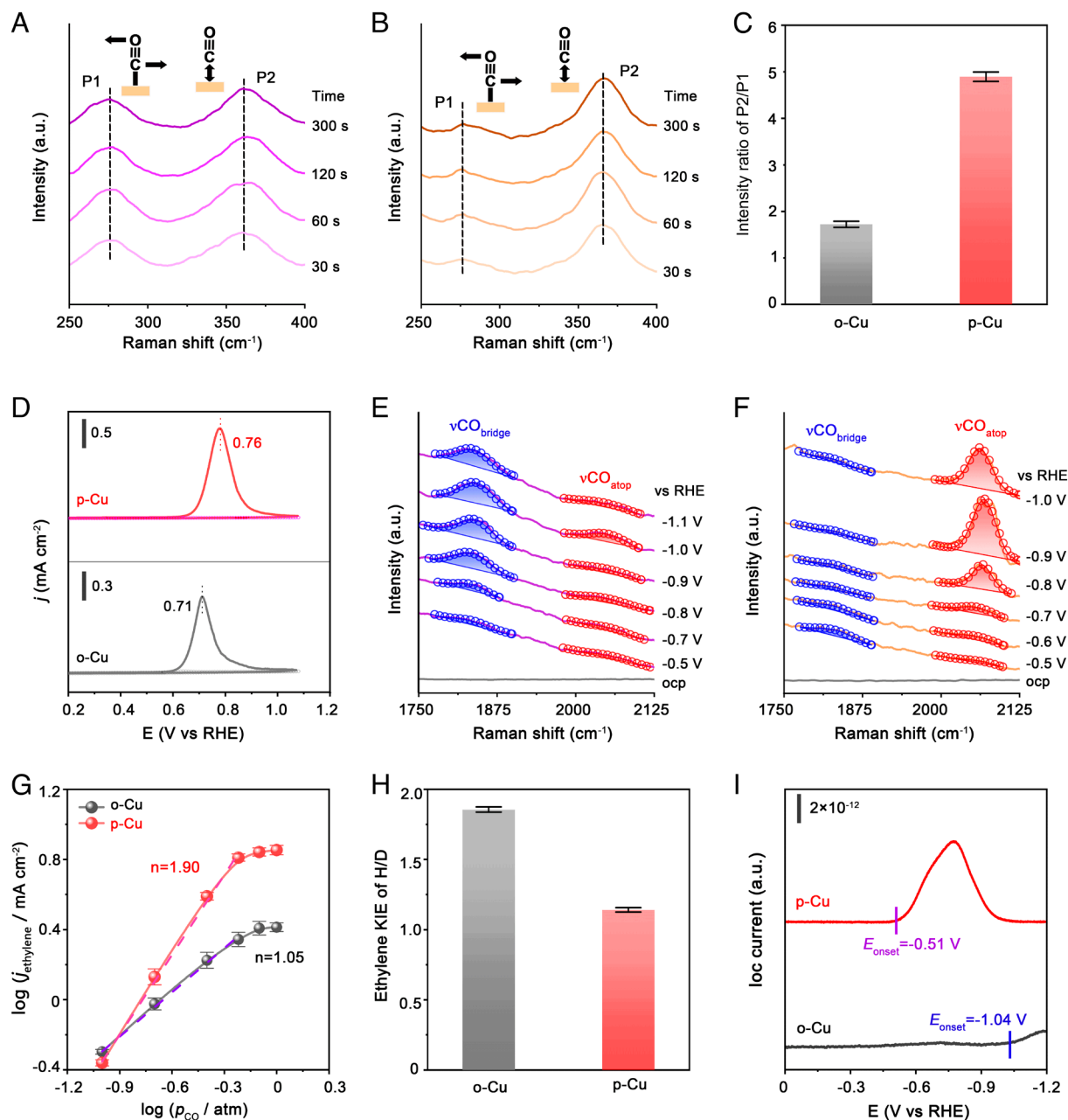
Fig. 4. In situ spectroscopic investigations and electrokinetic measurements. (*A* and *B*) In situ Raman spectra measured at 250 to 400 cm^{-1} on o-Cu (*A*) and p-Cu (*B*) at different reaction times under an applied potential of −1 V versus RHE. (*C*) Comparison of P2/P1 peak area ratio of o-Cu and p-Cu. (*D*) CO-stripping measurements on o-Cu and p-Cu. Sweep rate: 20 mV s^{-1}. (*E* and *F*) In situ Raman spectra on o-Cu (*E*) and p-Cu (*F*) as a function of applied potentials. (*G*) The logarithms of partial current densities for C_2H_4 formation versus logarithms of p_{CO}. (*H*) KIE of H/D in CO_2R to C_2H_4 performance. (*I*) Mass signals of C_2H_4 product (*m/z* = 26) on o-Cu and p-Cu as a function of applied potentials. Error bars are based on the SD of three independent measurements.

catalyst; whereas on Cu(111)-dominant Cu, the protonation of *CO with adsorbed H_2O becomes rate-limiting, thus leading to considerably different CO_2-to-C_2H_4 properties. Given the importance of elucidating reaction mechanisms on future catalyst development, our findings should offer insight into designing Cu-based catalysts for more selective C_2H_4 production via CO_2 electroreduction driven by renewable energy.

Materials and Methods

Synthesis of o-CuO Nanosheets. All chemicals were used as received with no further purification required. Cupric chloride dihydrate ($CuCl_2 \cdot 2H_2O$) and sodium hydroxide (NaOH) were purchased from Aladdin. First, 0.51 g $CuCl_2 \cdot 2H_2O$ was dissolved in 30 mL deionized water. Then, 30 mL of 3 M NaOH solution was added drop by drop to the $CuCl_2$ aqueous solution. The resulting mixture was

magnetically stirred for 30 min. The mixed solution was transferred into a 100 mL Teflon-lined stainless steel autoclave and heated at 100 °C for 10 h. After cooling to room temperature, the black sediment was collected by centrifugation. It was rinsed with DIW and ethanol and then dried at 60 °C for 3 h.

Synthesis of p-CuO Nanosheets. Briefly, 20 mg of dried o-CuO powder was spread evenly on an extended quartz boat (4 × 20 cm^2), which then was subjected to the N_2 plasma treatment in the chamber of the radio frequency-plasma enhanced chemical vapor deposition (RF-PECVD) systems under a pressure of 0.02 Torr. The radio frequency-plasma discharge was conducted at 100 W and 13.56 MHz for 30 min at room temperature. The dinitrogen (N_2, 99.999%) was purchased from Nanjing Special Gas Factory Co., Ltd. p-CuO samples were synthesized by changing the power and time of N_2 plasma process, which were denoted as at 50 W for 30 min: 50 W-30 min p-CuO; at 100 W for 15 min p-CuO: 100 W-15 min p-CuO; at 100 W for 30 min: 100 W-30 min (p-CuO, optimum

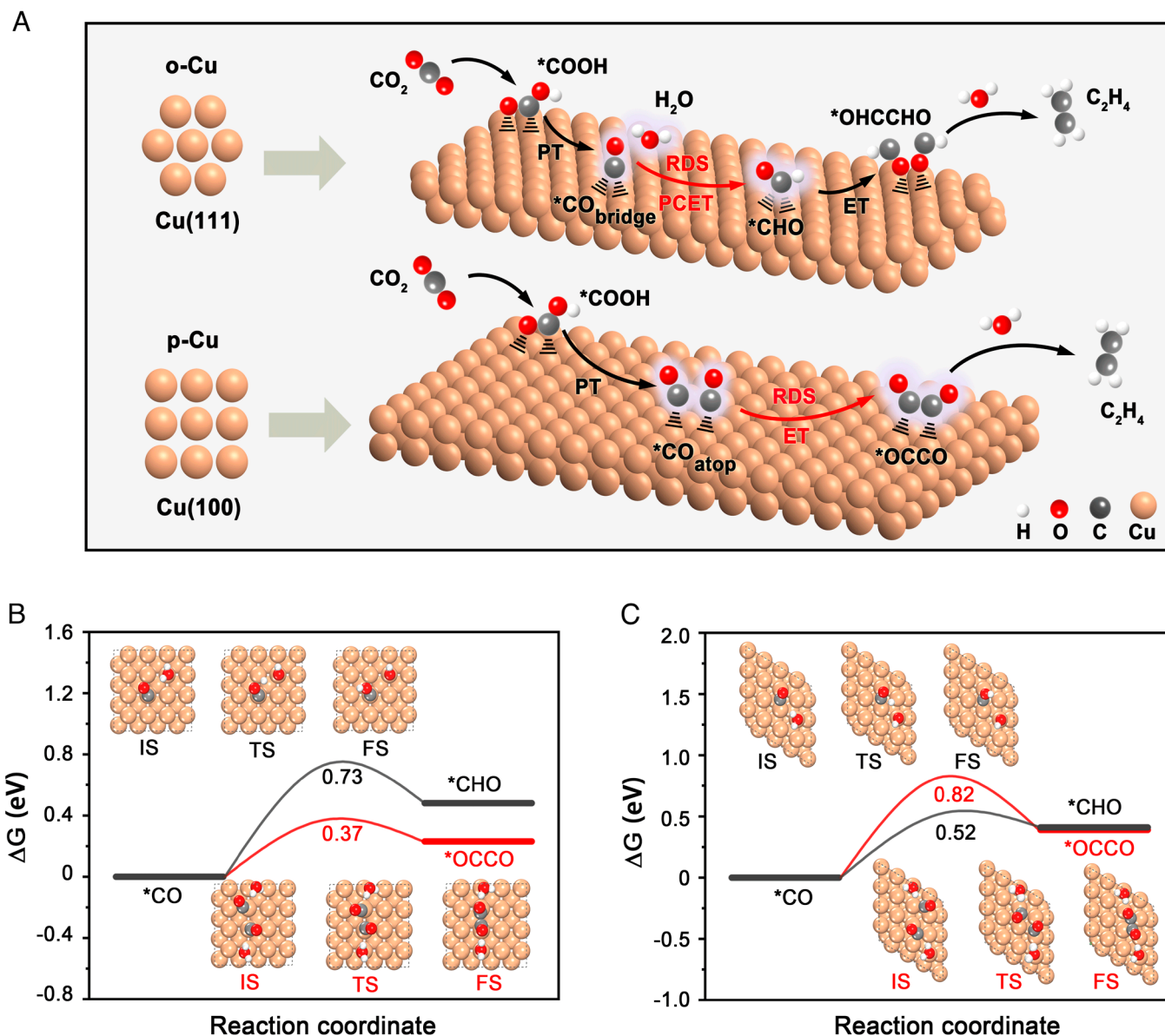**Fig. 5.** Facet-dependent RDS on Cu catalysts during CO$_2$-to-C$_2$H$_4$ conversion. (*A*) The proposed reaction mechanism for the CO$_2$R-to-C$_2$H$_4$ electroreduction on o-Cu and p-Cu. (*B* and *C*) The reaction-free energy barrier of the *CO→*OCCO and *CO→*CHO pathways on Cu(100) (*B*) and Cu(111) (*C*) facets. *Insets* present the models of the different reaction states on Cu(100) and Cu(111) facets. Initial state (IS); Transition state (TS); Final state (FS).

CO$_2$-to-C$_2$H$_4$ performance); at 100 W for 60 min: 100 W-60 min p-CuO; at 200 W for 30 min: 200 W-30 min p-CuO. (*SI Appendix*, Figs. S25 and S26).

Preparation of o-Cu/p-Cu Electrodes. Ten milligram o-CuO/p-CuO powder, 2 mL absolute ethyl alcohol, and 50 μL Nafion were mixed to form a catalyst ink by ultrasonic dispersion for at least 60 min. The obtained ink was then sprayed onto the YLS-30 T gas-diffusion layer (GDL) with an area of 3 × 3 cm^2 evenly. The electrodes were dried in a vacuum oven at room temperature for 2 h. The o-Cu and p-Cu electrodes were obtained by electrochemical reduction under 20 mA cm^{-2} current density for 10 min in a flow cell using the as-prepared catalysis. For the preparation of p-Cu electrodes, the CO$_2$ flow was kept constant at 50 mL min^{-1} controlled by a mass flow controller.

Material Characterizations. The as-synthesized catalysts were characterized by multiple analytic techniques. The morphology of the samples was determined by TEM [JEOL 2010F(s)]. The atomic-resolution HRTEM images, SAED, atomic-resolution HAADF images, and EDS elemental mapping were taken on a JEMARM 200F atomic-resolution analytical microscope with an acceleration voltage of 200 kV. XPS data were taken on ESCALab-MKII X-ray photoelectron spectrometer, Mg Kα radiation as the exciting source ($h\nu$ = 1,253.6 eV). ESR spectra were taken on the JEOL JES-FA200 electron spin resonance spectrometer (298 K, 9.062 GHz).

SAXS experiments were taken on Anton Paar GmbH SAXSpoint 2.0 Small angle X-ray scattering System. The KPFM characterizations were taken on Bruker Dimension Icon atomic force microscope. X-ray diffraction (XRD) patterns were taken on a Japan Rigaku DMax-γA X-ray diffractometer with Cu Kα radiation (λ = 1.54178 Å). Cu K-edge XAS spectra were carried out at the 1W1B beamline of Beijing Synchrotron Radiation Facility, China. Raman spectra were taken on the LabRAM HR Raman Spectrometer with a 633 nm excitation laser. DEMS spectra were taken on QMG 250 in situ differential electrochemical mass spectrometer.

Electrochemical Measurements. The electrochemical CO$_2$R tests were performed by a CHI 660e electrochemical workstation, which was equipped with a current amplifier. The prepared gas diffusion electrodes (GDEs) and IrO$_2$-coated Ti mesh were used as cathode and anode, respectively. Twenty milliliter catholytes (1 M KCl) and 20 mL anolytes (1 M KOH) were separated by a cation exchange membrane (Nafion 117). The CO$_2$ flow was kept constant at 50 mL min^{-1} controlled by a mass flow controller. In order to obtain accurate data, the gas flow rate at the outlet was monitored by a digital flowmeter. For the stability test, the electrolytes are periodically replaced with new 1 M KCl and 1 M KOH solutions, respectively. It was to recover the conductivity and ionic concentration of the test system. The applied potentials were measured against an Ag/AgCl reference electrode in

saturated KCl and converted to the RHE reference scale with iR_s correction by the following equation:

$$E \text{ (vs. RHE)} = E \text{ (vs. Ag/AgCl)} + 0.199 + (0.059 \times pH) - iR_s, \qquad [1]$$

where the solution resistance R_s was determined by electrochemical impedance spectroscopy (*SI Appendix*, Fig. S27).

In the MEA test, gaseous CO_2 passed through a 2.25×2.25 cm^2 gas chamber at the back side of GDL. The p-Cu evenly sprayed on the anion exchange membrane (sustain X37-50) and IrO_2-coated Ti mesh were used as cathode and anode, respectively. The anolytes (0.1 M $KHCO_3$) were heated in a water bath at 70 °C. For the stability tests, the anolytes were periodically replaced with new 0.1 M $KHCO_3$ solutions to recover the conductivity and ionic concentration.

Electrochemical OH⁻ Adsorption. The electrochemical OH⁻ adsorption was carried out in a N_2-saturated 1 M KOH electrolyte with a linear sweep voltammetry method at a sweep rate of 20 mV s^{-1}. The potential ranged from −0.4 to 0.7 V versus RHE for the o-Cu and p-Cu electrodes. The proportion of each surface was calculated by the OH⁻ adsorbed charge of each facet area of the fitted peaks on different catalysts. N_2 was continuously purged into the electrolyte during the measurement.

Electrochemical CO Stripping. For the CO stripping experiments, N_2 saturated 0.5 M $NaClO_4$ was used as the electrolyte. CO was then adsorbed onto the working electrode by continuously flowing high-purity CO into the cell for 15 min, while holding the potential at 0.1 V versus RHE. The gas was subsequently switched to N_2 for 30 min to purge traces of CO from the working electrode compartment. Cyclic voltammetry was then performed by sweeping the potential from 0.2 to 1.1 V versus RHE at 20 mV s^{-1}.

Reaction Order Measurement. The surface CO coverage can be controlled by changing the CO partial pressure in the H-type cell (24). In the partial pressure studies, the different CO partial pressures were achieved by mixing CO and N_2 gases at desired ratios using mass flow controllers after calibration. A 20 min electrolysis was conducted with an applied potential of −1 V versus RHE at each CO partial pressure starting from 1 atm. Then, the reaction products were sampled and the electrolysis was performed with the subsequent CO partial pressure. Error bars were based on the SD of three independent measurements.

Kinetic Isotope Effects of H/D. The kinetic isotopic effect (KIE) of H/D over the catalysts was measured with a similar procedure except for replacing H_2O with D_2O. The electrodes were electrolyzed for 20 min at an applied potential of −1 V versus RHE, and then the reaction products were sampled. Error bars were based on the SD of three independent measurements.

In Situ Raman Spectroscopy Measurement. A three-electrode Spectro-electrochemical flow cell was used for in situ Raman scattering spectroscopy measurements. The GDEs were used as the work electrode, a saturated Ag/AgCl as the reference electrode, and a graphite rod as the counterelectrode. The anode and cathode compartments were separated by a Nafion membrane to avoid cross-contamination. During the tests, CO_2 gas was passed through the back side of the GDE. The Raman tests were taken on LabRAM HR Raman Spectrometer equipped with a 633 nm excitation laser. Signal acquisition time for each spectrum was about 30 s.

In Situ DEMS Measurement. DEMS spectra were taken on QMG 250 in situ differential electrochemical mass spectrometer. A cold trap cooled with dry ice is installed between the vacuum chamber and the electrochemical cell to trap the water vapor during the experiments to avoid potential damage to the mass spectrometer. The working electrode is an Au film sputtered on a porous polytetrafluoroethylene (PTFE) membrane. The catalyst ink was directly dropped into the Au film and then dried at room temperature. The hydrophobic PTFE membrane permits gas flow while rejecting liquid. A piece of carbon paper (YLS-30 T) and a saturated Ag/AgCl were used as the counterelectrode and

reference electrode, respectively. The anode and cathode compartments were separated by a Nafion membrane to avoid cross-contamination. Background signals of the DEMS were collected by prerunning for 20 min. Then, the prepared electrodes performed the LSV cycle in the potential range of 0 to −1.2 V versus RHE at a scan rate of 1 mV s^{-1}.

Density Functional Theory Calculations. The plane-wave code Vienna ab initio simulation package (VASP) program (54) was employed to perform all the spin-polarized DFT calculations within the generalized gradient approximation (GGA) using the Perdew–Burke–Ernzerhof (PBE) formulation (55) with dispersion correction based on the DFT-D3 scheme. The projected augmented wave (PAW) potentials (56) were chosen to describe the ionic cores and take valence electrons into account using a plane wave basis set with a kinetic energy cutoff of 500 eV. Partial occupancies of the Kohn−Sham orbitals were allowed using the Gaussian smearing method and a width of 0.02 eV. The electronic energy was considered self-consistent when the energy change was smaller than 10^{-6} eV.

The Cu(100), Cu(111), and CuO(001) surface model slab was separated by a 15 Å vacuum layer in the z direction between the slab and its periodic images. During structural optimizations of the surface models, a $3 \times 3 \times 1$ gamma-point centered k-point grid for the Brillouin zone was used. All the atomic layers were allowed to fully relax.

To study the *CO→*OCCO and *CO→*CHO reaction pathways, its energy barriers were determined by using the climbing image nudged elastic band method. The Gibbs free energy is calculated by:

$$G = H - T\Delta S = E_{DFT} + E_{ZPE} - TS, \qquad [2]$$

where E_{DFT} is the total energy from the DFT calculation. E_{ZPE} is the zero-point energy, S is the entropy and T is the temperature. The vibrational analysis, limited to the surface adsorbates and keeping the rest of the system fixed, was carried out for zero-point energy and entropy corrections by calculating a Hessian matrix with a finite difference approach with a step size of 0.02 Å.

The adsorption energy (E_{ads}) of an adsorbate A was defined as:

$$E_{ads} = E_{ads/surf} - E_{surf} - E_{ads}, \qquad [3]$$

where $E_{ads/surf}$, E_{surf}, and E_{ads} are the energy of the adsorbates adsorbed on the surface slab, the energy of surface slab, and the energy of adsorbates respectively.

The surface energy ($E_{surface}$) was used as defined below:

$$E_{surface} = \frac{(E_{total} - nE_{ref} - E_{ads})}{2A}, \qquad [4]$$

where E_{total} is the total energy of this surface from DFT calculations; E_{ref} is the reference energy of unit composition from bulk calculation; E_{ads} is the sum of the adsorption energies of the intermediates at given coverages; A is the surface area; and n is the number of unit composition in this surface. Given this definition, the more positive the surface energy is for a surface, the less stable this surface is.

Data, Materials, and Software Availability. All study data are included in the article and/or *SI Appendix*.

1. B. Franco *et al.*, Ethylene industrial emitters seen from space. *Nat. Commun.* **13**, 6452 (2022).
2. Z. Huang, R. G. Grim, J. A. Schaidle, L. Tao, The economic outlook for converting CO_2 and electrons to molecules. *Energy Environ. Sci.* **14**, 3664–3678 (2021).
3. I. E. Agency, CO_2 emissions in 2022 (International Energy Agency, www.iea.org, 2023).
4. Y. Liang *et al.*, Stabilizing copper sites in coordination polymers toward efficient electrochemical C-C coupling. *Nat. Commun.* **14**, 474 (2023).
5. C. Chen, Y. Li, P. Yang, Address the "alkalinity problem" in CO_2 electrolysis with catalyst design and translation. *Joule* **5**, 737–742 (2021).

6. B. Zhang *et al.*, Highly electrocatalytic ethylene production from CO(2) on nanodefective Cu nanosheets. *J. Am. Chem. Soc.* **142**, 13606–13613 (2020).

7. P. Wei *et al.*, Coverage-driven selectivity switch from ethylene to acetate in high-rate CO(2)/CO electrolysis. *Nat. Nanotechnol.* **18**, 299–306 (2023).

8. W. Ren, A. Xu, K. Chan, X. Hu, A cation concentration gradient approach to tune the selectivity and activity of CO_2 electroreduction. *Angew. Chem. Int. Ed.* **61**, e202214173 (2022).

9. I. Roh *et al.*, Photoelectrochemical CO_2 reduction toward multicarbon products with silicon nanowire photocathodes interfaced with copper nanoparticles. *J. Am. Chem. Soc.* **144**, 8002–8006 (2022).

10. W. Liu *et al.*, Electrochemical CO(2) reduction to ethylene by ultrathin CuO nanoplate arrays. *Nat. Commun.* **13**, 1877 (2022).

11. C. Chen *et al.*, Oxidation of metallic Cu by supercritical CO_2 and control synthesis of amorphous nano-metal catalysts for CO2 electroreduction. *Nat. Commun.* **14**, 1092 (2023).

12. Y. Wang *et al.*, Catalyst synthesis under CO_2 electroreduction favours faceting and promotes renewable fuels electrosynthesis. *Nat. Catal.* **3**, 98–106 (2019).

13. Z. Gu *et al.*, Efficient electrocatalytic CO_2 reduction to C2+ alcohols at defect-site-rich Cu surface. *Joule* **5**, 429–440 (2021).

14. Y. H. Wang *et al.*, In situ Raman spectroscopy reveals the structure and dissociation of interfacial water. *Nature* **600**, 81–85 (2021).

15. W. Ma *et al.*, Electrocatalytic reduction of CO_2 to ethylene and ethanol through hydrogen-assisted C-C coupling over fluorine-modified copper. *Nat. Catal.* **3**, 478–487 (2020).

16. M. Zhong *et al.*, Accelerated discovery of CO(2) electrocatalysts using active machine learning. *Nature* **581**, 178–183 (2020).

17. J. Chen *et al.*, Accelerated transfer and spillover of carbon monoxide through tandem catalysis for kinetics-boosted ethylene electrosynthesis. *Angew. Chem. Int. Ed.* **62**, e202215406 (2023).

18. C. T. Dinh *et al.*, CO2 electroreduction to ethylene via hydroxide-mediated copper catalysis at an abrupt interface. *Science* **360**, 783–787 (2018).

19. X. Zhang *et al.*, Selective and high current CO(2) electro-reduction to multicarbon products in near-neutral KCL electrolytes. *J. Am. Chem. Soc.* **143**, 3245–3255 (2021).

20. Z. Wang *et al.*, Localized alkaline environment via in situ electrostatic confinement for enhanced CO(2)-to-ethylene conversion in neutral medium. *J. Am. Chem. Soc.* **145**, 6339–6348 (2023).

21. Y. N. Xu *et al.*, Tuning the microenvironment in monolayer MgAl layered double hydroxide for CO2-to-ethylene electrocatalysis in neutral media. *Angew. Chem. Int. Ed.* **62**, e202217296 (2023).

22. C. Choi *et al.*, Highly active and stable stepped Cu surface for enhanced electrochemical CO_2 reduction to C_2H_4. *Nat. Catal.* **3**, 804–812 (2020).

23. W. Ren, W. Ma, X. Hu, Tailored water and hydroxide transport at a quasi-two-phase interface of membrane electrode assembly electrolyzer for CO electroreduction. *Joule* **7**, 1–12 (2023).

24. X. Chang *et al.*, C−C coupling is unlikely to be the rate-determining step in the formation of C_{2+} products in the copper-catalyzed electrochemical reduction of CO. *Angew. Chem. Int. Ed.* **61**, e202111167 (2021).

25. J. Li *et al.*, Electrokinetic and in situ spectroscopic investigations of CO electrochemical reduction on copper. *Nat. Commun.* **12**, 3264 (2021).

26. G. Kastlunger *et al.*, Using pH dependence to understand mechanisms in electrochemical CO reduction. *ACS Catal.* **12**, 4344–4357 (2022).

27. A. Wagner, C. D. Sahm, E. Reisner, Towards molecular understanding of local chemical environment effects in electro- and photocatalytic CO_2 reduction. *Nat. Catal.* **3**, 775–786 (2020).

28. A. T. Chu, Y. Surendranath, Aprotic solvent exposes an altered mechanism for copper-catalyzed ethylene electrosynthesis. *J. Am. Chem. Soc.* **144**, 5359–5365 (2022).

29. E. Perez-Gallent, G. Marcandalli, M. C. Figueiredo, F. Calle-Vallejo, M. T. M. Koper, Structure- and potential-dependent cation effects on CO reduction at copper single-crystal electrodes. *J. Am. Chem. Soc.* **139**, 16412–16419 (2017).

30. F. Calle-Vallejo, M. T. M. Koper, Theoretical considerations on the electroreduction of CO to C2Species on Cu(100) electrodes. *Angew. Chem. Int. Ed.* **52**, 7282–7285 (2013).

31. Y. Wang, J. Liu, G. Zheng, Designing copper-based catalysts for efficient carbon dioxide electroreduction. *Adv. Mater.* **33**, e2005798 (2021).

32. C. Chen *et al.*, Exploration of the bio-analogous asymmetric C-C coupling mechanism in tandem CO2 electroreduction. *Nat. Catal.* **5**, 878–887 (2022).

33. Z. Z. Wu *et al.*, Identification of Cu(100)/Cu(111) interfaces as superior active sites for CO dimerization during CO(2) electroreduction. *J. Am. Chem. Soc.* **144**, 259–269 (2022).

34. K. J. Schouten, Z. Qin, E. Perez Gallent, M. T. Koper, Two pathways for the formation of ethylene in CO reduction on single-crystal copper electrodes. *J. Am. Chem. Soc.* **134**, 9864–9867 (2012).

35. G. Zhang *et al.*, Efficient CO(2) electroreduction on facet-selective copper films with high conversion rate. *Nat. Commun.* **12**, 5745 (2021).

36. J. Y. Kim *et al.*, Quasi-graphitic carbon shell-induced Cu confinement promotes electrocatalytic CO(2) reduction toward C(2+) products. *Nat. Commun.* **12**, 3765 (2021).

37. Y. Lin *et al.*, Tunable CO_2 electroreduction to ethanol and ethylene with controllable interfacial wettability. *Nat. Commun.* **14**, 3575 (2023).

38. Y. Zhao *et al.*, Elucidating electrochemical CO_2 reduction reaction processes on Cu(hkl) single-crystal surfaces by in situ Raman spectroscopy. *Energy Environ. Sci.* **15**, 3968–3977 (2022).

39. H. Li *et al.*, C_{2+} selectivity for CO_2 electroreduction on oxidized Cu-based catalysts. *J. Am. Chem. Soc.* **145**, 14335–14344 (2023).

40. Z. Geng *et al.*, Oxygen vacancies in ZnO nanosheets enhance CO_2 electrochemical reduction to CO. *Angew. Chem. Int. Ed.* **57**, 6054–6059 (2018).

41. Z. Gu *et al.*, Oxygen vacancy tuning toward efficient electrocatalytic CO_2 reduction to C_2H_4. *Small Methods* **3**, 1800449 (2018).

42. J. Zhao, R. Liu, Z. Hua, Hydrothermal synthesis and optical properties of single crystalline CuO nanosheets. *Superlattices Microstruct.* **81**, 243–247 (2015).

43. C. Liu *et al.*, Enhanced photocatalytic degradation performance of BiVO4/BiOBr through combining Fermi level alteration and oxygen defect engineering. *Chem. Eng. J.* **449**, 137757 (2022).

44. Y. Tong *et al.*, Oxygen vacancies confined in nickel molybdenum oxide porous nanosheets for promoted electrocatalytic urea oxidation. *ACS Catal.* **8**, 1–7 (2017).

45. Z. Ma *et al.*, CO(2) electroreduction to multicarbon products in strongly acidic electrolyte via synergistically modulating the local microenvironment. *Nat. Commun.* **13**, 7596 (2022).

46. S. Jiang, K. Klingan, C. Pasquini, H. Dau, New aspects of operando Raman spectroscopy applied to electrochemical CO_2 reduction on Cu foams. *J. Chem. Phys.* **150**, 041718 (2019).

47. C. Zhan *et al.*, Revealing the CO coverage-driven C-C coupling mechanism for electrochemical CO(2) reduction on Cu(2)O nanocubes via operando Raman spectroscopy. *ACS Catal.* **11**, 7694–7701 (2021).

48. X. Chang *et al.*, Understanding the complementarities of surface-enhanced infrared and Raman spectroscopies in CO adsorption and electrochemical reduction. *Nat. Commun.* **13**, 2656 (2022).

49. A. M. Limaye, J. S. Zeng, A. P. Willard, K. Manthiram, Bayesian data analysis reveals no preference for cardinal Tafel slopes in CO_2 reduction electrocatalysis. *Nat. Commun.* **12**, 703 (2021).

50. T. Zhang, B. Yuan, W. Wang, J. He, X. Xiang, Tailoring *H intermediate coverage on the CuAl2O4/CuO catalyst for enhanced electrocatalytic CO_2 reduction to ethanol. *Angew. Chem. Int. Ed.* **62**, e202302096 (2023).

51. K. J. P. Schouten, E. Pérez Gallent, M. T. M. Koper, The influence of pH on the reduction of CO and CO2 to hydrocarbons on copper electrodes. *J. Electroanal. Chem.* **716**, 53–57 (2014).

52. Y. Ma *et al.*, Confined growth of silver-copper janus nanostructures with 100 facets for highly selective tandem electrocatalytic carbon dioxide reduction. *Adv. Mater.* **34**, e2110607 (2022).

53. Z. Yin *et al.*, Cu3N nanocubes for selective electrochemical reduction of CO_2 to ethylene. *Nano Lett.* **19**, 8658–8663 (2019).

54. G. Kresse, J. Hafner, Ab initiomolecular dynamics for liquid metals. *Phys. Rev. B* **47**, 558–561 (1993).

55. J. P. Perdew, K. Burke, M. Ernzerhof, Generalized gradient approximation made simple. *Phys. Rev. Lett.* **77**, 3865 (1996).

56. P. E. Blöchl, Projector augmented-wave method. *Phys. Rev. B* **50**, 17953–17979 (1994).